DNA-origami line-actants control domain organisation and fission in synthetic membranes

Roger Rubio-Sánchez,[1, 2, 3, 4, *] Bortolo Matteo Mognetti,[5] Pietro Cicuta,[4] and Lorenzo Di Michele[1, 2, 3, 4, †]

[1] *Department of Chemical Engineering and Biotechnology, University of Cambridge,*
Philippa Fawcett Drive, Cambridge CB3 0AS, United Kingdom
[2] *Department of Chemistry, Molecular Sciences Research Hub,*
Imperial College London, London W12 0BZ, United Kingdom
[3] *fabriCELL, Molecular Sciences Research Hub, Imperial College London, London W12 0BZ, United Kingdom*
[4] *Biological and Soft Systems, Cavendish Laboratory, University of Cambridge,*
JJ Thomson Avenue, Cambridge CB3 0HE, United Kingdom
[5] *Interdisciplinary Center for Nonlinear Phenomena and Complex Systems,*
Université libre de Bruxelles (ULB), Campus Plaine,
CP 231, Blvd. du Triomphe, B-1050 Brussels, Belgium

Cells can precisely program the shape and lateral organisation of their membranes using protein machinery. Aiming to replicate a comparable degree of control, here we introduce DNA-Origami Line-Actants (DOLAs) as synthetic analogues of membrane-sculpting proteins. DOLAs are designed to selectively accumulate at the line-interface between co-existing domains in phase-separated lipid membranes, modulating the tendency of the domains to coalesce. With experiments and coarse-grained simulations we demonstrate that DOLAs can reversibly stabilise two-dimensional analogues of Pickering emulsions on synthetic giant liposomes, enabling dynamic programming of membrane lateral organisation. The control afforded over membrane structure by DOLAs extends to membrane three-dimensional morphology, as exemplified by a proof-of-concept synthetic pathway leading to vesicle fission. With DOLAs we lay the foundations for replicating, in synthetic systems, some of the critical membrane-hosted functionalities of biological cells, including signalling, trafficking, sensing, and division.

Biological membranes coordinate numerous pathways critical to life, from trafficking to signal transduction and cellular motility [1], many of which rely on regulating the distribution and interactions of membrane machinery. Among other regulatory principles, cells are believed to exploit membrane phase separation and critical composition fluctuations to dynamically generate local heterogeneity [2–10]. Cell membranes are also known to contain inclusions that can accumulate at the line-interface between co-existing lipid domains [11–15], and relax the associated line tension [16–18]. It has been proposed that cells use these *line-actants* as an additional means to dynamically control membrane phase behaviour and the lateral organisation of membrane inclusions [19] underpinning, for instance, the function of signalling hubs [20, 21] and the generation of endo/exosomes [22, 23].

Artificial cell science aims to construct, from the bottom-up, synthetic analogues of biological cells that mimic their sophisticated behaviours [24, 25], and are expected to widely impact next generation diagnostics, therapeutics and bioprocessing [26–28]. Often constructed from lipid bilayers [29], synthetic cell membranes have been engineered to replicate an array of biomimetic responses [30], including mechanotransduction [31], energy conversion [32–34], and membrane deformation [35]. In parallel to solutions relying on reconstituted membrane proteins [32–34], fully synthetic DNA nano-devices, anchored to the bilayers by means of hydrophobic tags, have emerged as a versatile toolkit for biomembrane engineering [36–38], having enabled the design of biomimetic pathways for transport [39–41], trafficking [42, 43], cell adhesion [44, 45], tissue formation [46–48], signal detection [49], membrane remodelling [50–53], and surface patterning [54–56].

Despite these advances, the design of pathways enabling systematic control over the local structure and composition of synthetic cell membranes, to the same degree of what is afforded by extant biological machinery, remains an elusive task.

Here we introduce DNA-Origami Line-Actants (DOLAs) as a means of controlling the formation, stability and three-dimensional morphology of lipid domains on synthetic bilayers. Leveraging the modularity of amphiphilic DNA nanotechnology [54], DOLAs have been designed to selectively accumulate at the line-interface between co-existing domains on Giant Unilamellar Vesicles (GUVs). Using a combination of experiments and coarse-grained simulations, we show that, similar to interfacial inclusions in three dimensions, DOLAs can modulate the tendency of lipid domains to coalesce, stabilising two-dimensional analogues of Pickering emulsions. The devices can be de-activated upon exposure to a molecular stimulus, triggering domain coarsening and unlocking the sought dynamic control over lateral membrane organisation. Combined with osmotic unbalance, we demonstrate that DOLAs can form the basis of a synthetic pathway leading to membrane budding-off and fission, exemplifying three-dimensional morphological control.

Owing to their modular design and robust working

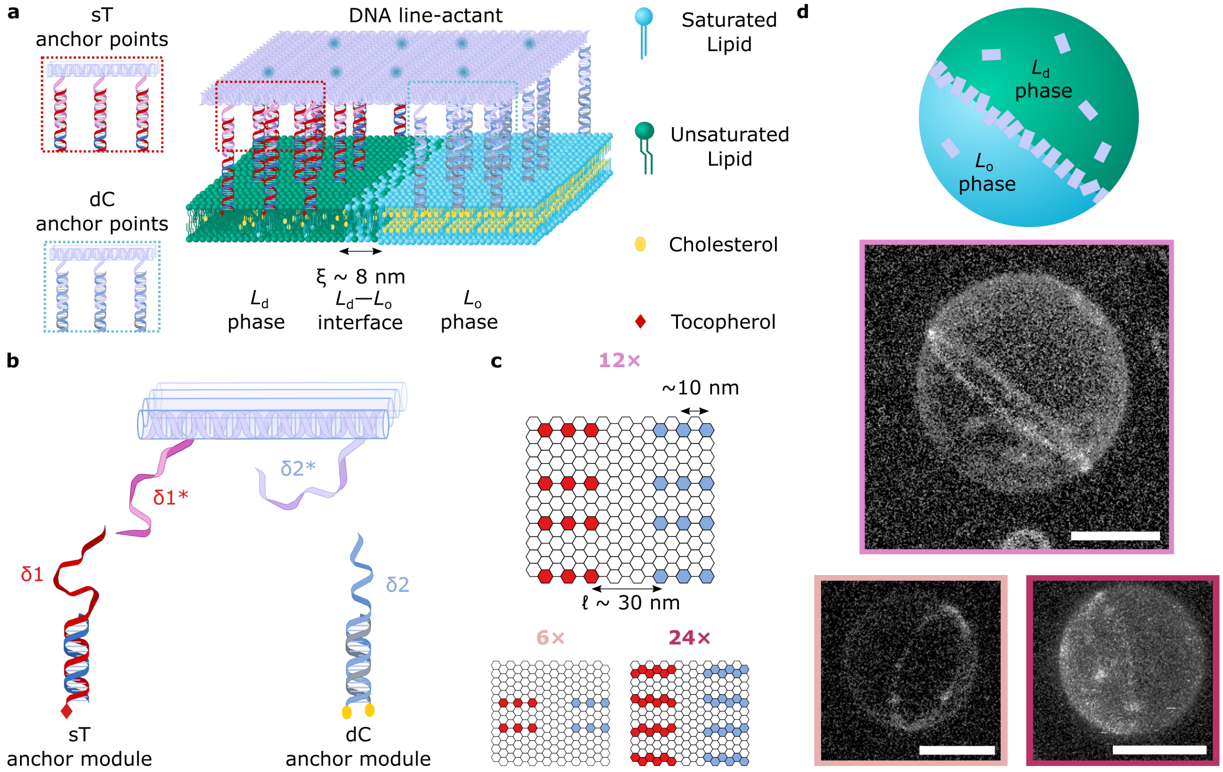

FIG. 1. **DNA-origami line-active agents enrich the line-interface of phase-separated GUVs. a** Schematic representation of a multi-component lipid bilayer membrane composed of saturated and unsaturated lipids mixed with sterols, displaying liquid-ordered (L_{o}) and liquid-disordered (L_{d}) phase co-existence. The outer leaflet of the membrane is decorated with a DNA-origami line-actant (DOLA), where amphiphilic anchor-modules bearing single-tocopherol (sT) and double-cholesterol (dC) motifs enrich their preferred (L_{d} and L_{o}, respectively) phases, driving accumulation of the DOLA at the $L_{\mathrm{d}} - L_{\mathrm{o}}$ interface. **b** Selected staples on the origami were extended to include overhang domains $\delta1^*$ and $\delta2^*$, with complementarity to dC (blue) or sT (red) anchor modules, respectively. **c** Hexagonal grids depict the arrangement of staples across the origami plates, where each hexagon corresponds to the 3' terminus of a staple. We positioned sets of 6× (light pink), 12× (pink), or 24× (magenta) overhangs targeting the same type of anchor-points. The two sets of anchors are separated by a distance $\ell \sim 30\,\mathrm{nm}$ (6× and 12×) or $\ell \sim 25\,\mathrm{nm}$ (24×). **d** (Top) Schematic representation a de-mixed GUV where the $L_{\mathrm{d}} - L_{\mathrm{o}}$ interface is enriched with DOLAs. (Bottom) 3D views of phase-separated vesicles with a Janus-like morphology showing line-accumulation of fluorescent (Alexa488) 6× (light pink), 12× (pink), or 24× (magenta) DOLAs, as reconstructed from a confocal z-stack using Volume Viewer (FIJI [57]) with contrast enhancement (see Supplementary Fig. 3 for reconstructions without contrast enhancement). Scale bars = 10 μm.

principle, we argue that DOLAs could constitute a versatile toolkit for synthetic-cell membrane engineering, allowing us to take full advantage of the rich phenomenology of lipid phase separation and design ever-more advanced membrane-hosted functionalities.

RESULTS AND DISCUSSION

Engineering line-actants with DNA nanostructures

Our design of choice for DNA line-actants, depicted schematically in Fig. 1a, exploits the versatility of the Rothemund Rectangular Origami (RRO) as a "molecular breadboard", featuring an array of regularly spaced binding sites [58–61]. The rectangular tiles (Supplementary Fig. 1) feature two sets of either 6, 12 or 24 single-stranded (ss) DNA overhangs extended from the same face of the origami, as shown in Fig. 1b. The sticky ends, with sequence $\delta1^*$ or $\delta2^*$, can respectively bind complementary overhangs on double-stranded (ds) DNA *anchoring modules* functionalised with two cholesterol moieties (dC) or a single tocopherol (sT) [54]. We have recently determined that dC and sT modules display, respectively, thermodynamic preferences for accumulating within liquid-ordered (L_{o}) and liquid-disordered (L_{d}) domains of phase-separated membranes. Specifically, transporting a dC module from L_{d} to L_{o} produces a moderately favourable free-energy shift ($\Delta G^{\mathrm{dC}}_{\mathrm{p},L_{\mathrm{o}}}$) of $\sim -0.8\,k_{\mathrm{B}}T$, while sT has a stronger affinity for disordered domains ($\Delta G^{\mathrm{sT}}_{\mathrm{p},L_{\mathrm{o}}} \approx 1.9\,k_{\mathrm{B}}T$) [54]. The two sets of dC and sT modules were distributed on opposite halves of the tiles, with spacing of $\ell \sim 30\,\mathrm{nm}$ between the two distinct sets of anchors (Fig. 1b). Because ℓ is comfortably greater than the width of the boundary separating L_o and L_d phases, estimated as $\xi \sim 8\,\text{nm}$ (Supplementary Note I), free energy minimisation is expected to drive the accumulation of the tiles across line interfaces, accommodating each set of anchors in their respective preferred phase (Fig. 1a). We produced three DOLA designs, with either 6×, 12× or 24× anchors of each type, expecting an increase in the free energy gain associated to line accumulation for larger number of anchors (Fig. 1c).

DOLAs were further labelled with fluorescent (Alexa488) beacons, located on the face opposite to that hosting the anchors (Supplementary Fig. 2), thus allowing us to monitor their distribution by means of confocal microscropy. Accumulation of the three DOLA designs at the L_d–L_o line-interface in phase-separated GUVs (DOPC/DPPC/Chol 2:2:1) is demonstrated in Fig. 1d with confocal 3D reconstructions, where the equatorial boundary separating the two hemispherical domains is clearly delineated by the fluorescent plates.

A custom-built image segmentation and analysis routine, detailed in Supplementary Note II and Supplementary Fig. 4, was applied to the confocal data to sample the fluorescence intensity profile of DOLAs across the line interface, as sketched in Fig. 2a. The resulting curves, shown in Fig. 2b, display clear peak at the L_d–L_o boundary location ($x = 0$), confirming line-interface accumulation. As detailed in Supplementary Note II, fitting of the diffraction-limited fluorescent peak and baseline signals from the surrounding L_d and L_o regions allowed us to estimate a line-partitioning coefficient $K_{\text{p,int}}$, defined as the ratio between the surface density of origami at the line-interface and the average origami surface density on the entire GUV.

Figure 2c summarises the experimentally determined $K_{\text{p,int}}$ for the three tested designs, rendering similar results for the 12× and 24× tiles, with and a slightly larger value for the 6× variant. Line-interface adsorption models, outlined in Supplementary Note III (see associated Supplementary Fig. 5), enable the estimation of $K_{\text{p,int}}$ for the three DOLA designs. We fitted the theoretical estimates to experimentally determined $K_{\text{p,int}}$ values, using the overall surface coverage of the origami on the GUVs, σ, as fitting parameter. The obtained estimates of $1.5 < \sigma^{12\times}_{\text{theory}} < 9.3\%$ and $2.9 < \sigma^{24\times}_{\text{theory}} < 14.4\%$ for 12× and 24×, respectively, are in good agreement with the nominal experimental surface coverage $\sigma_{\text{exp}} \sim 5\%$ (Supplementary Fig. 6). For the 6× design, we estimated $\sigma^{6\times}_{\text{theory}} < 3.2\%$, slightly below the nominal experimental value and reflecting the larger observed $K_{\text{p,int}}$ and the smaller absolute fluorescence intensity values (see Supplementary Note III and Supplementary Fig. 7). A smaller than expected σ is likely the result of a decreased membrane-affinity, given the fewer anchor-points available for the 6× tiles.

Fitted line-adsorption models allowed us to estimate the fraction of the line-interface occupied by DOLAs, ϕ

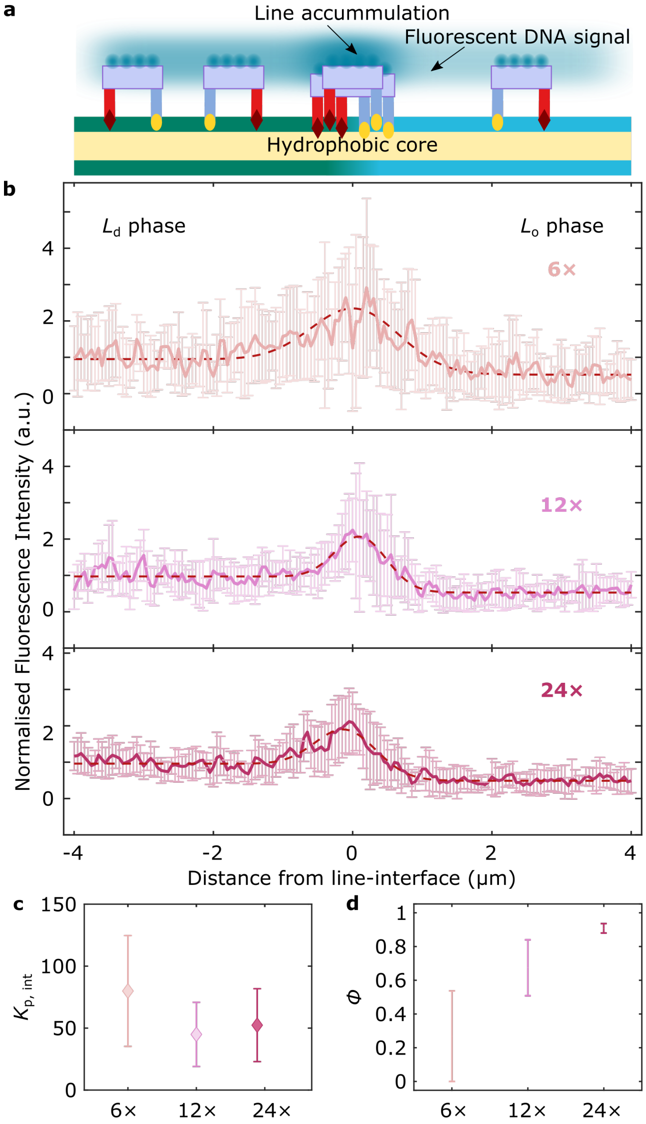

FIG. 2. **Line-accumulation of DOLAs is regulated by the number of anchors.** **a** Schematic depiction of a demixed lipid membrane decorated with DOLAs, where fluorescent Alexa488 beacons enable the quantification of origami distribution from fluorescence intensity profiles (Supplementary Note II). **b** Line-interface accumulation conveyed by plots of average fluorescence intensities ± standard deviation across line-interfaces decorated with 6×, 12×, or 24× DOLAs. The profiles, as a function of distance from the line-interface ($x = 0$), have been normalised to the mean L_d-phase intensity. Red dashed lines are fits to Eq. S2 (Supplementary Note II), which models the experimental, diffraction-blurred, fluorescence intensity profile. **c** Line-partitioning coefficients ($K_{\text{p,int}}$) of DOLAs featuring sets of either 6×, 12×, or 24× dC/sT anchor-points. **d** Fraction of line-interface occupied (ϕ) by 6×, 12×, or 24× line-actants, computed using the experimental $K_{\text{p,int}}$ in our numerical line-adsorption model (see Supplementary Note III and Supplementary Figs. 5, 6, and 7.)

(see definition in Supplementary Note III and Supplementary Fig. 5), summarised in Fig. 2d. Expectedly, we note an increase in ϕ with increasing number of anchors, with the strongly-binding 24× approaching saturation and the 6× leaving much of the line unoccupied, hence demonstrating control over the degree of line-actant accumulation by design.

DOLAs stabilise two-dimensional Pickering emulsions

Having demonstrated that DOLAs can programmably accumulate at the boundary between co-existing lipid phases, we sought to verify whether this accumulation leads to stabilisation of the line-interface, as hypothesised for biological line actants [14]. To this end, we decorated the phase-separating GUVs with 12× DOLAs at a nominal surface coverage of $\sim$ 30%, so to further promote line-interface saturation ($\phi \sim 0.75 - 0.87$). The GUVs, fluorescently labelled with L_d-partitioning Texas Red-DHPE for ease of visualisation, were heated to $\sim 37^\circ$C, well above their miscibility transition temperature of $T_\mathrm{m} \sim 33\pm1^\circ$C [63], to induce lipid mixing. After incubating at high temperature for ~ 5 minutes, the sample was quenched back to room temperature ($T = 25^\circ$C), leading to the nucleation of L_o or L_d domains in a background of the opposite phase.

In non-functionalised GUVs, the domains rapidly coarsen until most vesicles display two quasi-hemispherical domains, resulting in Janus-like morphologies (Fig. 3a, bottom). However, in DOLA-functionailsed GUVs, coalescence was arrested leading to morphologies with a large number of small, stable domains, analogous to two-dimensional Pickering emulsions (Fig. 3a, top). To quantify the domain-stabilising ability of DOLAs, we analysed epifluorescence micrographs collected $\sim$ 3 hrs after quenching, and extracted the fraction F of non-Janus vesicles, namely those that failed to relax into the two-domain morphology. Results, summarised in Fig. 3b, clearly demonstrate how most line-actant decorated GUVs display Pickering morphologies (Fig. 3a, top). In turn, the Janus morphology is dominant when GUVs lack either the dC or the sT anchor modules, no tiles are included, or if the origami are prepared omitting the overhangs to target either dC or sT. The latter controls confirm that domain stabilisation emerges solely thanks to line-interface accumulation of the rationally designed DOLAs, rather than as a result of non-specific effects associated to the individual membrane inclusions.

As further confirmation that domain stabilisation is underpinned by interfacial accumulation of the origami, vesicles lacking TexasRed-lipids and decorated with fluorescent DOLAs were subjected to an analogous heating-cooling program and inspected with confocal microscopy. Besides detecting domain stabilisation, line-accumulation was confirmed at the boundaries of the stabilised lipid domains, as demonstrated in Fig. 3c with a 3D view from a confocal z-stack reconstruction.

Coarse grained simulations capture DOLA line accumulation and domain stabilisation

To further validate our line-actant engineering strategy, we conducted Monte Carlo (MC) simulations using a coarse-grained representation of the experimental system. As presented in Fig. 4a, and detailed in Supplementary Note IV, we defined a two-dimensional Ising model on a triangular lattice, which displays phase co-existence at sufficiently low temperature. We interpret the phase rich in spin $s = 1$ (green) as L_d, and that rich in $s = -1$ (blue) as L_o. Rectangular tiles were included with anchor-points arranged on the lattice according to their nominal position on the DOLAs. The interaction free energies between dC/sT anchors and their lipid micro-environment were modelled in the system's Hamiltonian as $J_\mathrm{dC}\cdot\tilde{s}$ and $J_\mathrm{sT}\cdot\tilde{s}$, respectively, where $\tilde{s}$ is the sum of the spins over the lattice site hosting the anchor and its six nearest neighbours ($\tilde{s} \in [-7, -5, ..., 5, 7]$). The anchor-coupling constant values were chosen as $J_\mathrm{sT} = 0.136\, k_\mathrm{B}T$ and $J_\mathrm{dC} = -0.057\, k_\mathrm{B}T$, reflecting the experimentally-determined partitioning free energies of the modules (see Supplementary Note IV and ref. [54]).

To replicate the experimental protocol, we prepared high temperature systems with uniform spin (and tile) distributions, before quenching to a lower temperature at which de-mixing occurs. The quenching temperature was chosen to replicate the experimental line tension of $\sim 1\,$pN [62] (see Supplementary Note IV). The system was simulated with Kawasaki dynamics [64], conserving the number of $s = -1$ and $s = 1$ spins, initially set to a ratio of 2/3. The tiles, present at a surface coverage $\sigma = 30\%$, readily localised at the boundaries of the blue domains emerging after quenching, leading to their stabilisation, as shown in Fig. 4b (see also Supplementary Movie 1). Figure 4c compares the time-evolution of systems featuring and lacking 12× tiles. When tiles were present, coarsening was slowed down and small domains persisted at the end of the simulation run ($t_\mathrm{MC} = 2\times10^7$ steps). Conversely, over the same time window, the system lacking the tiles achieved complete coarsening, resulting in a morphology with one domain of each phase, analogous to the Janus GUVs (Supplementary Movies 2 and 3, respectively). Supplementary Fig. 9 compares frequency histograms of the number of domains in 15 runs at various t_MC, confirming the ability of the tiles to slow down domain coarsening, in line with experimental findings outlined in Fig. 3.

Despite its coarse-grained nature, simulations offer insights on the different mechanisms leading to domain coarsening, and on how these are influenced by the pres-

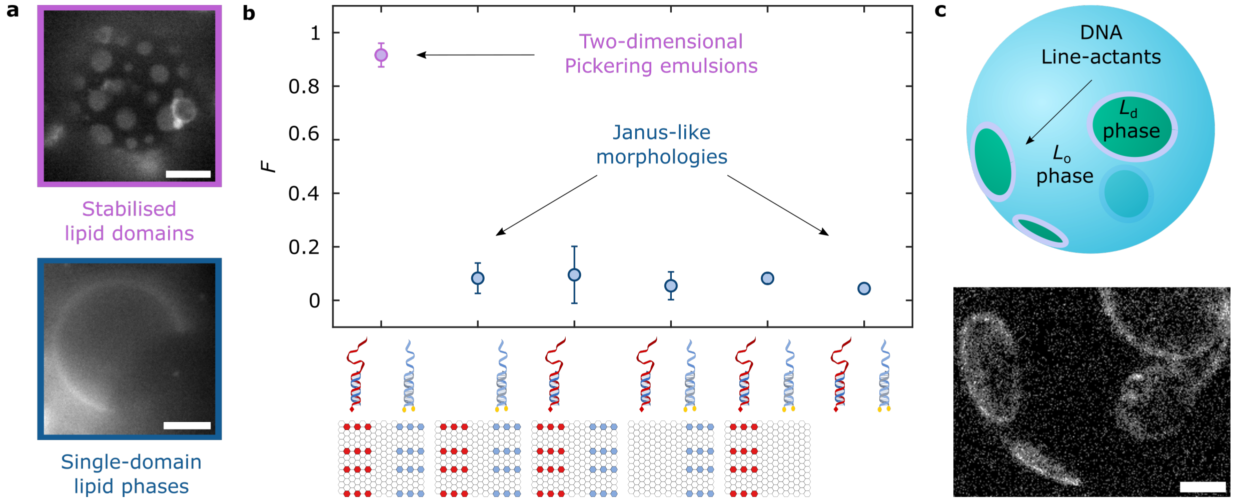

FIG. 3. **DOLAs stabilise two-dimensional analogues of Pickering emulsions.** **a** Representative epifluorescence micrographs of de-mixed GUVs showing: (top) stable lipid domains ≈ 3 hours after phase separation in the presence of 12× DOLAs; (bottom) GUV lacking line-actants that equilibrated to produce a Janus morphology with two quasi-hemispherical L_d and L_o domains. Fluorescent marker is Texas Red-DHPE, which partitions to the L_d phase. Scale bars = 10 μm. **b** Programmable, domain-stabilising, activity of DOLAs as conveyed by the fraction, F, of GUVs exhibiting more than two domains with respect to that of Janus vesicles. As shown in the graphical legend, besides the complete DOLAs, we exploited the modularity of the platform to produce various control functionalisation schemes expected to lack line-active behaviour, including omitting either sT or dC modules, using tiles that lack overhangs targeting sT or dC, and omitting tiles altogether. **c** Line-accumulation of DOLAs scaffolds lipid domains and confers them with stability against coalescence, as shown with a 3D view of a reconstructed vesicle after heating above and quenching below the miscibility transition temperature. Interfacial accumulation of fluorescent (Alexa488) 12× DOLAs readily shows stable domains rendered from a confocal z-stack using Volume Viewer (FIJI [57]) with contrast enhancement (see Supplementary Fig. 8 for reconstructions without contrast enhancement). Scale bar = 10 μm.

ence of DOLAs. Generally, we observed that coarsening occurs following two distinct pathways: domain coalescence and Ostwald ripening [65]. Simulations suggest that the presence of the tiles slows down the former mechanism, by offering a steric barrier that prevents the interfaces of two distinct domains from coming in sufficient proximity and undergo coalescence. Instead, Ostwald ripening, supported by the exchange of particles (spins) between domains *via* diffusion through the background phase, occurs regardless of the presence of tiles. This second coarsening process is solely responsible for the decrease in total line-length observed in the presence of tiles at very long simulation times (Fig. 4d, inset), when no further domain coalescence is observed. In experiments, tile-decorated GUVs display stable 2D Pickering emulsions ∼ 3 hours after quenching, when most non-functinonalised vesicles have already fully equilibrated (Fig. 3b), hinting that domain coalescence may be the primary mechanism leading to coarsening, with Ostwald ripening playing a comparatively minor role.

Figure 4d compares the simulated time-evolution of the overall line-interface length (L) for systems featuring the three DOLA designs with those lacking tiles. At late simulation times, the interface length is higher for 24×, followed by 12× and 6×, with the latter design showing values identical to the tile-less control, confirming the expected link between number of anchors and line-stabilising ability. See also Supplementary Fig. 10 and the associated Supplementary Movies 4 and 5 for representative simulation runs with 24× and 6× DOLAs.

Consistently, as shown in Fig. 4e, the simulated tile-occupied fraction of the line (ϕ) converges to values that monotonically increase with the number of anchors, in agreement with the experimental/theoretical findings outlined in Fig. 2e. Analogous trends are noted when monitoring the time-dependent fraction of tiles at the line-interface, found to increase with the number of anchors (Supplementary Fig. 12). Further insights can be gathered from Fig. 4f, where we plot the fraction of tiles at the line as a function of interface length. We note that, as L decreases due to domain coarsening, strongly binding 24× tiles remain more persistently pinned at the interface, while 6× tiles are readily expelled. Finally, in Fig. 4g, we explicitly explore the correlation between ϕ and the line length. As L shrinks, a plateau in ϕ is approached for 6× DOLAs, able to readily desorb from the line. In turn, a correlation is retained for strongly-pinned 24× DOLAs.

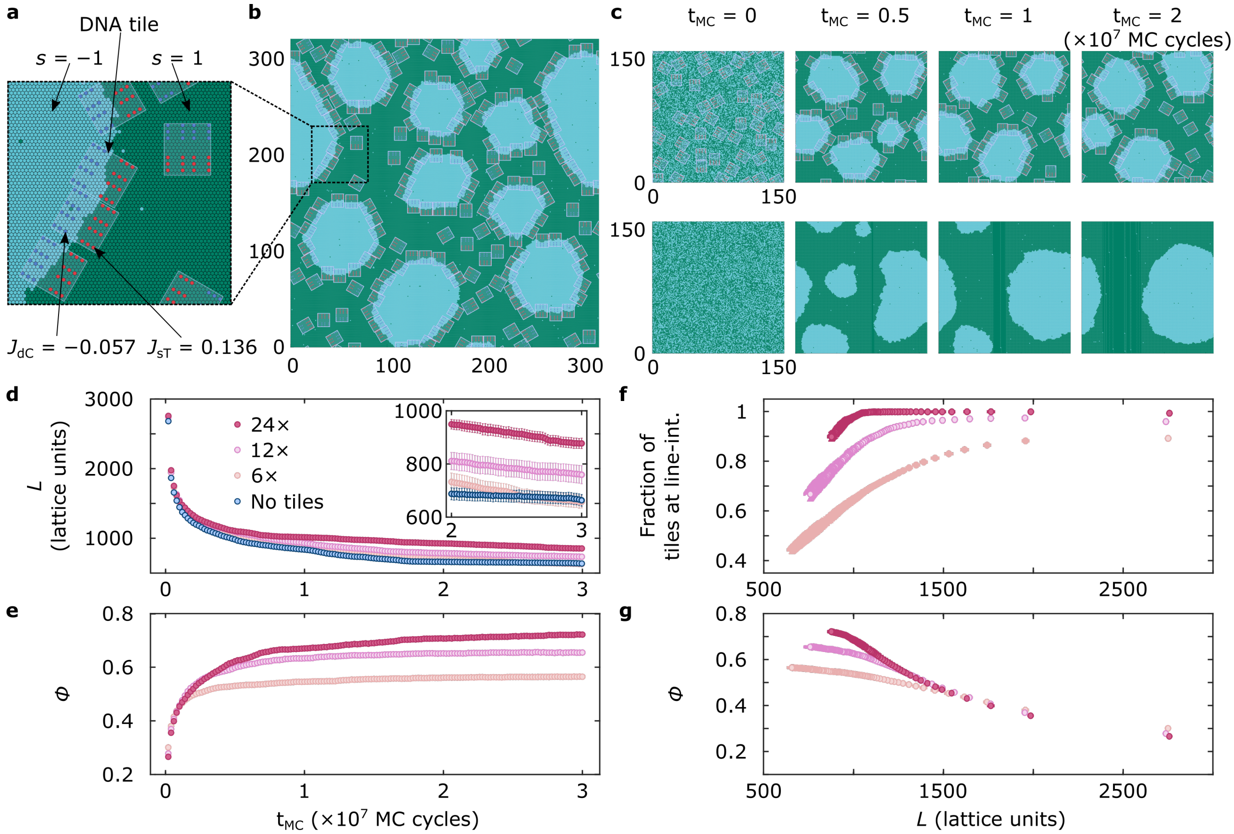

FIG. 4. **Coarse-grained simulations replicate DOLA line-accumulation and domain stabilisation.** **a** Representation of the developed Ising model with hexagonal unit cells carrying spins of $s = 1$ (green) and $s = -1$ (blue). Neighbouring spins interact through a coupling parameter $J = 0.55\,k_\mathrm{B}T$, chosen to roughly replicate the expected experimental line tension $\sim 1\,\mathrm{pN}$ [62]. Anchor-points on the tiles are arranged based on the 12× DOLA design. Each anchor is located at an Ising lattice point and contributes with a free-energy term $J_\mathrm{x} \sum_{i=1}^{7} s_i$, where s_i indicates the spins of the lattice point hosting the anchor and the 6 nearest neighbors, and J_x is a coupling constant taking different values for sT ($J_\mathrm{sT} = 0.136\,k_\mathrm{B}T$) and dC ($J_\mathrm{dC} = -0.057\,k_\mathrm{B}T$) to account for the different partitioning tendencies. **b** Representative snapshot of a simulation trajectory after $t_\mathrm{MC} = 2\,(\times 10^7\mathrm{MC\ cycles})$, where tiles stabilise blue domains by accumulating at their boundary. Box size: 320 × 372 lattice points. **c** Snapshots exemplifying the time-evolution of representative simulations, one including 12× DOLAs, where multiple domains retain stability even after $t_\mathrm{MC} = 2 \times 10^7$MC cycles (top), and the second lacking tiles and equilibrating to form a single domain (bottom). Box size: 160×172 lattice points. **d** Time dependence of the overall length of the line-interface (L) in simulations containing the three tested DOLA designs or no tiles, quantifying DOLA-induced interface stabilisation. **e** Line-accumulation of 6×, 12×, and 24× DOLAs conveyed by the time-evolution of fraction of line-interface (ϕ) occupied by tiles. A tile is said to be at the line when featuring at least 80% of favourable anchor-spin interactions relative to the total contacts (Supplementary Fig. 11)) **e** Fraction of the tiles present in the system located at the interface, showing that designs remain pinned at the line more readily as the latter shrinks. **f** Fraction of the line-interface (ϕ) occupied by tiles as a function of line length (L). The monotonic decrease is sharper for stronger-binding tiles.

Fueling lipid domain re-organisation with dynamic DNA line-actants

The ability of DOLAs to regulate domain coarsening can be readily coupled to nanostructure re-configurability afforded by toeholding reactions [66, 67], thus enabling dynamic control over membrane lateral organisation. To demonstrate this functionality, we modified the 12× line-actants with a 6-nt toehold domain of sequence α on the 3'-end of cholesterol-targeting overhangs. As depicted schematically in Fig. 4a, a chemical Fuel, in the form of an oligonucleotide with sequence $\alpha^*\delta 2$, can selectively displace the dC anchoring modules from the tile through a toeholding reaction (see Supplementary Fig. 13 for an agarose gel electrophoresis confirming the sought molecular response). When removing the dC anchors, DOLAs are expected to lose their affinity for the line-interface and instead partition to L_d driven by the remaining sT moieties, negating the ability of the tiles to stabilise lipid domains.

As sketched in Fig. 4b (left), and shown in Fig. 4c (left) with fluorescence micrographs, GUVs decorated with the responsive versions of the 12× tiles form stable 2D emulsions when subjected to the heating-cooling

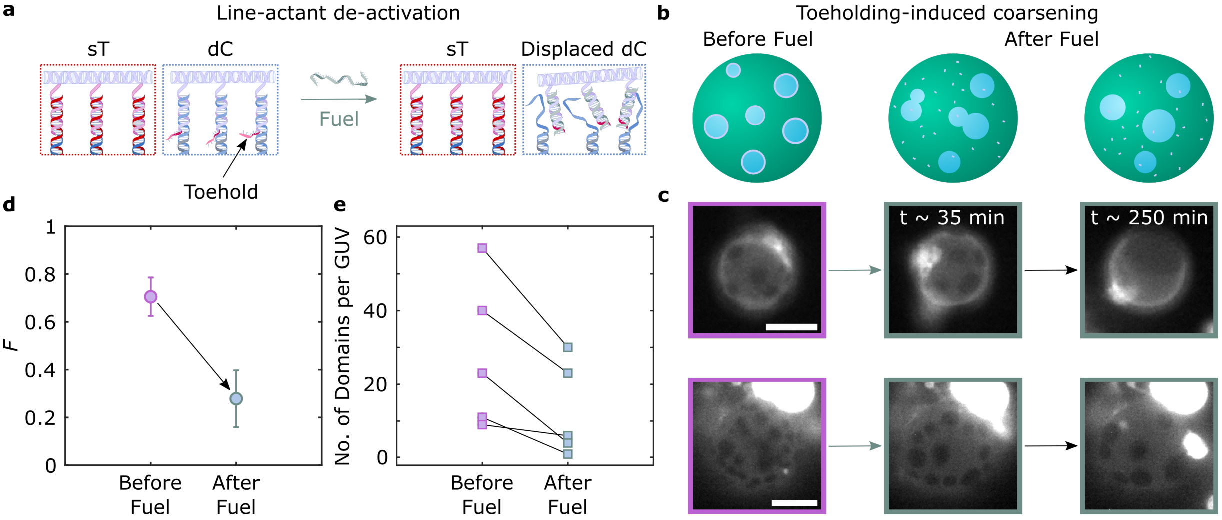

FIG. 5. **Toehold-mediated strand displacement enables dynamic control over membrane lateral organisation *via* DOLA reconfiguration. a** Schematic depiction of anchor-points in DOLAs, highlighting the toehold domain linked to the dC-targeting overhangs. The addition of a Fuel strand catalyses a strand displacement reaction, detaching the DNA tile from the anchor-points and leading to DOLA de-activation. **b** DOLA re-configuration, and their subsequent desorption from line-interfaces, lead to domain coarsening. **c** Representative epi-fluorescence micrographs acquired before and after ($\sim$ 35 and $\sim$ 250 minutes) the addition of Fuel, demonstrating domain coarsening triggered by DOLA de-activation. Fluorescent marker is Texas Red-DHPE, which partitions to the L_d phase. Scale bars = 10 μm. **d** Influence of DOLA re-configuration on the fraction, F, of GUVs exhibiting more than two domains with respect to that of Janus-like vesicles before and after ($\sim$ 250 minutes) the addition of Fuel. **e** Number of domains per GUV in representative vesicles, showing the effect of toeholding before and after ($\sim$ 250 minutes) the addition of Fuel. Points connected by lines are relative to the same GUV.

cycle outlined above. Figures 4b–c (centre and right) show domain coarsening triggered by exposure to the Fuel strand, which translates into a clear decrease in the fraction F of non-Janus GUVs, shown in Fig. 4d. The series of snapshots in Fig. 4c shows that, while some GUVs acquire a two-domain Janus morphology after Fuel exposure (top), others retain a larger number of domains. Nonetheless, all observed GUVs experience a substantial degree of domain coarsening, as outlined in Fig. 4e where we track changes in the number of domains following Fuel addition in individual GUVs. As exemplified in Supplementary Fig. 14, domains often bulge after fuel addition, possibly due to a slight osmolarity mismatch coupled with differences in spontaneous curvature between the phases. Bulging may in turn be responsible for enhancing stability against coalescence of the domains after line-actant de-activation, preventing some GUVs from relaxing into the Janus configuration [68].

Responsive DOLAs for domain fission in synthetic membranes

The ability of DOLAs to reversibly stabilise domains can be exploited to synthetically replicate the action of biological membrane-remodelling machinery, tackling a critical bottleneck in synthetic cell engineering [69]. For instance, phospholipase A_2 has been postulated to exhibit enhanced catalytic activity at line-interfaces between co-existing L_o and L_d phases, driving domain budding and fission [70]. We propose that our line-actants could form the basis of an analogous pathway coordinating fission and, therefore, three-dimensional membrane transformation.

We started by preparing GUVs in an initial configuration featuring DOLA-stabilised micro-domains, as outlined above. We then applied an hyper-osmotic shock by increasing the osmolarity of the outside solution (C_O) to $\sim 1.28 \times C_I$, where C_I is the internal osmolarity of the GUVs, thus leading to an increase in GUV excess area [71]. While in some cases the osmotic shock led to membrane internalisation (Supplementary Fig. 15), some domains responded by bulging-out, as schematically depicted in Fig. 6a and experimentally observed in Fig. 6b. At this stage, some bulged-out domains could be “primed” for complete budding-off or fission, driven by minimisation of the line-interface energy and opposed by membrane fluctuation entropy [72] and, possibly, steric repulsion between DOLAs preventing line shrinkage. Deactivation of the line-actants through Fuel strand addition is expected to increase line tension and negate any steric hinderance to interface shrinkage, tipping the marginally stable domains into full budding off and fission, as depicted in Fig. 6c (top). Fission events can be

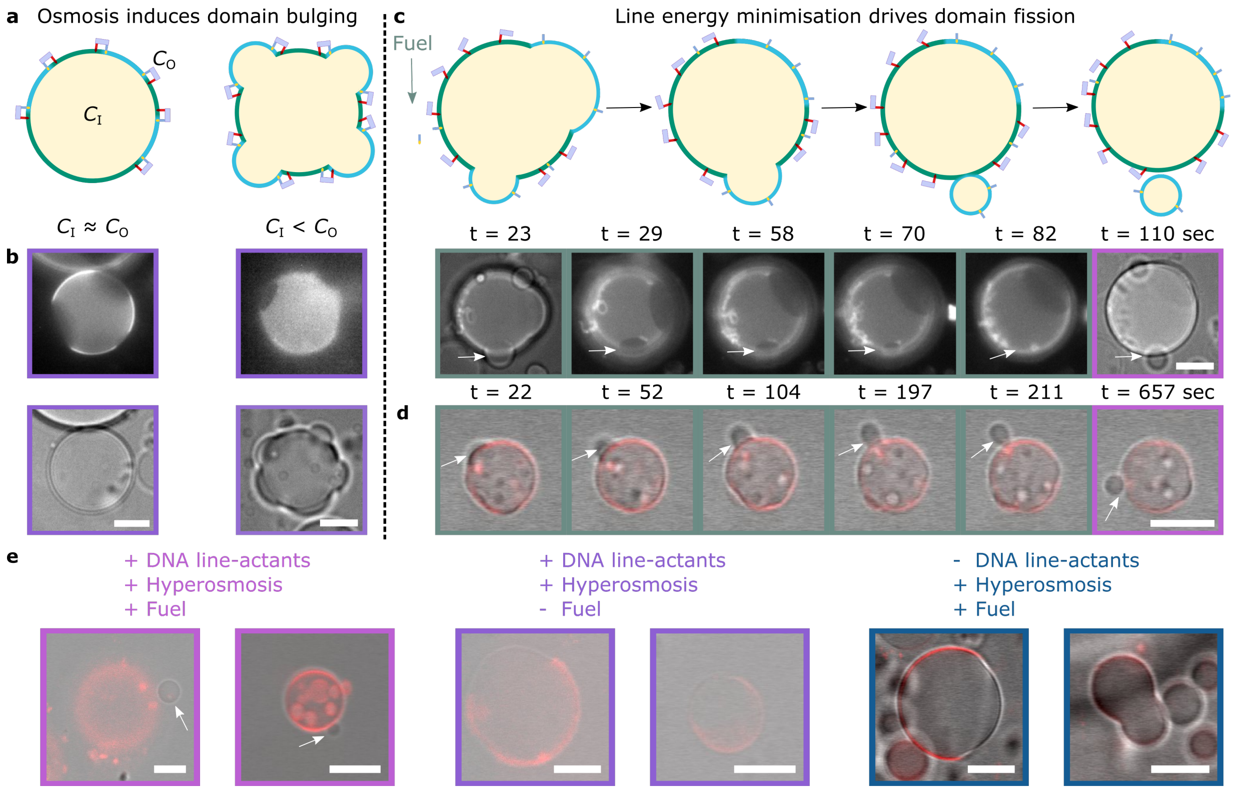

FIG. 6. **Biomimetic fission pathway mediated by DOLAs.** The fission mechanism requires two sequential processes: domain budding and domain fission. **a** Schematic representation of the first step, where bulging-out of DOLA-stabilised domains is caused by hyperosmotic shock, *i.e.* by increasing the outer concentration of solutes (C_O) relative to the concentration inside the GUVs (C_I). **b** Epifluorescence (Top) and brightfield (bottom) micrographs of representative GUVs exposed to iso-osmolar ($C_I \approx C_O$) or hyper-osmolar ($C_I < C_O$) environments, showing respectively spherical or bulging-out morphologies. **c** (Top) Schematic depiction of the second step, where Fuel addition and tile desorption from the interfaces induce budding off or fission of the protruding domains. (Bottom) Evolution of L_o-domain fission in a representative liposome observed with brightfield and epifluorescence microscopy (see Supplementary Movie 6). Time-staps refer to the time elapsed after initial acquisition. Fuel was added ~ 2 minutes before acquisition began. **d** Evolution of L_o-domain fission in a representative GUV shown with overlaid confocal and bright field images (see Supplementary Movie 7). Time-staps refer to the time elapsed after initial acquisition. Fuel was added ~ 90 minutes before acquisition began. **e** Overlaid confocal and bright field micrographs of representative liposomes when exposed to: hyper-osmotic environments containing Fuel (Left) or lacking Fuel (Middle), or in the presence of Fuel but lacking DNA line-actants (Right). Fluorescent marker is Texas Red-DHPE, which partitions to the L_d phase. All scale bar $= 10\,\mu$m.

promptly recorded experimentally upon Fuel-strand addition, as shown in Supplementary Movie 6 and Fig. 6c (bottom). The sequence of epifluorescence images in the latter clearly shows the dark region corresponding to a budding L_o-domain shrinking progressively, and ultimately disappearing. Vesicle fission is confirmed with brightfield micrographs, where arrows highlight both the parent and "daughter" vesicles regaining spherical morphologies. An analogous example is provided in Fig. 6d, and the associated Supplementary Movie 7, with overlaid confocal and bright-field micrographs.

In further support of our proposed synthetic fission pathway, DOLA-functionalised liposomes with stabilised micro-domains were gently added to imaging wells containing hyper-osmotic buffer baths with and without Fuel. In the former scenario, confocal microscopy revealed further examples of phase-separated GUVs found in proximity of a smaller single-phase vesicle (Fig. 6e, left, and Supplementary Fig. 16), similar to the confirmed fission occurrences shown in Fig. 6c and d. In turn, we did not observe such presumed fission events in vesicles immersed in buffer baths lacking Fuel (Fig. 6e, middle), where GUVs appeared more Janus-like, also in line with our findings on sample heterogeneity summarised in Supplementary Fig. 15. Finally, DOLA-lacking GUVs, immersed in Fuel-supplemented hyper-osmotic buffer, simply adopted dumb-bell shapes thanks to their Janus-morphology (Fig. 6e, right), consistent with the expectation that the used C_O/C_I is insufficient to drive fission of quasi-hemispherical domains [73].

CONCLUSIONS AND OUTLOOK

In summary, we presented the first example of a rationally designed nanostructure - dubbed DOLAs - capable of accumulating at the one-dimensional line-interface between lipid domains, imitating biological line-active membrane inclusions. The synthetic line-actants exploit the programmability and modularity of DNA origami, combined with the natural tendency of cholesterol and tocopherol "anchors" to enrich distinct lipid phases. Through experiments and numerical modelling, we demonstrated that the affinity for line-interfaces can be programmed by tuning the number of hydrophobic anchors, thus proposing a general design principle readily applicable to different origami designs, hydrophobic groups, or membrane compositions. We further demonstrated that our line-actants are able to stabilise small lipid domains against coarsening, giving rise to two-dimensional analogues of Pickering emulsions on the surface of giant liposomes, and achieving a previously unattainable degree of control over the lateral organisation of synthetic bilayers. The nano-devices can be externally de-activated through a simple toehold-mediated strand displacement operation, triggering domain coalescence. Coarse-grained Monte-Carlo simulations replicate the experimental phenomenology, identifying origami-origami steric repulsion as the primary mechanism leading to domain stabilisation, and ultimately validating our line-actant engineering strategy. Finally, we combined externally-triggered line-actant deactivation with osmotic unbalance to implement a proof-of-concept synthetic fission pathway, whereby offspring liposomes programmably bud-off from parent vesicles, demonstrating the ability of the nano-devices to promote large-scale membrane re-structuring similar to biological nanomachines [23, 74, 75].

The simplicity and modularity of the mechanism underpinning line-action in our devices points at straightforward possible design variations to exploit different origami geometries, anchor chemistry, and polymerisation approaches to further program the number, size and morphology of lipid domains, marking a conceptual shift in synthetic-membrane engineering. Responsiveness to a wider range of physical and chemical stimuli can also be achieved by incorporating active elements such as DNAzymes [76], G-quadruplexes [77], aptamers [78], and/or photo-actuable moieties (e.g. azobenzene) [79], thus broadening the design space and applicability of synthetic membrane re-structuring pathways.

Thanks to their ability to program membrane restructuring and the lateral distribution of membrane inclusions, the DOLAs constitute a valuable toolkit in synthetic-cell science that could underpin elusive and highly sough-after behaviours such as synthetic cell division, vesicle-based trafficking and signal transduction pathways, ultimately unlocking disruptive applications to advance therapeutics and diagnostics.

DOLAs or similar devices could be used to achieve previously unattainable control over the local domain structure of live cell membranes. One could thus envisage applying the origami line-actant toolkit as the basis of biophysical studies aimed a clarifying the role of microphase separation in cell signalling, by triggering the formation and disruption of "lipid rafts" at will [20]. If strong correlations between disease-related pathways and membrane-domain structure are established, the origami line-actants could provide a new means for conditioning cell behaviour carrying potential therapeutic value.

METHODS

Electroformation of Phase-separating Giant Unilamellar Vesicles

Electroformed vesicles [63, 80] were prepared in a 300 mM sucrose solution in MilliQ water as reported previously [54]. Briefly, lipid mixtures composed of 1,2-dioleoyl-sn-glycero-3-phosphocholine (DOPC, chain melting temperature -17°C; Avanti Polar Lipids), 1,2-dipalmitoyl-sn-glycero-3-phosphocholine (DPPC, chain melting temperature 41°C; Avanti Polar Lipids), and cholestanol (Sigma-Aldrich) at 4:4:2 molar ratio. In addition, fluorescent Texas Red-DHPE (Invitrogen) was included in the lipid mixtures at 0.8% molar ratio, which preferentially enriches L_d domains. Subsequently, 45 μL of lipid mixtures (4 mg$\cdot$ mL^{-1}) were spread on the conducting side of clean indium tin oxide (ITO) slides heated above 60°C. The slides were placed in a dry silica dessicator for $\sim$1 hour and then assembled into an electroformation chamber using a $\sim$1 mm thick polydimethylsiloxane (PDMS) spacer enclosing approximately 400 μL of degassed sucrose buffer. Electroformation chambers were placed in a pre-heated oven at $T > 60$°C and connected to a frequency generator using clamps. The electroformation program consisted of a sinusoidal alternating current (AC), voltage amplitude of 2V, and frequency of 10 Hz for 2 hrs followed by 2 Hz for 1 hr. Finally, vesicles were retrieved and stored at room temperature in the dark to prevent photo-bleaching and photo-oxidation.

Design of line-active DNA origami nano-devices

DNA anchoring modules were designed using the NUPACK suite software [81], and are based on previously reported nano-devices [49, 54]. For the line-active plates, we used a modified version of the Rothemund Rectangular Origami [82]. Membrane attachment was achieved by functionalising the origami plates with the Picasso software [58], which allowed to precisely engineer the spatial location of membrane-anchoring points. To that end, the sequence of specific staples was extended on their 3' end to include docking domains that would project outwards on a single face of the planar origami. These overhangs hybridised to sticky-end overhangs of DNA-based anchoring modules. On the opposite face of the origami, 5' end extensions were incorporated in eight DNA staples to include a domain capable of binding a fluorescent oligonucleotides for confocal imaging. In the case of line partitioning experiments, 5'-end extensions were used to attach a strand with 3× binding sites for fluorescent oligonucleotides, in order to increase the signal-to-noise upon confocal acquisition.

Assembly of DNA Nanostructures

Lyophilised DNA oligonucleotides (Integrated DNA Technologies [IDT], Eurogentec, and Biomers), were reconstituted to a nominal concentration of 100 μM in Tris-Ethylenediaminetetraacetic acid (EDTA) buffer (1× TE: 10 mM Tris + 1 mM EDTA, pH 8.0).

DNA anchor-modules were subjected to a slow quenching temperature ramp on a TC-512 thermal cycler (95°C down to 4°C at a rate of -0.5°C min $^{-1}$) in a buffer containing 1× TE + 100 mM NaCl.

Origami plates self-assembled with a temperature quenching ramp in a total volume of 100 μL containing 7249-bp single-stranded circular viral template (M13mp18, tilibit nanosystems) as scaffold (10 nM) as well as core and modified stapling oligonucleotides, in the presence of a folding buffer composed of 1× TE + 12.5 mM $MgCl_2$. Staples capable of membrane attachment were included at 100× excess, while core staples as well as those part of the fluorescent beacon were present at a 10× excess.

Thermal annealing was performed in a TC-512 thermal cycler. Samples were incubated at 80°C for 5 minutes to promote denaturing and suppress secondary structures. Subsequently, the temperature was decreased to 60°C, and later on to 40°C with a rate of $0.3125°\mathrm{C} \cdot \mathrm{min}^{-1}$. Finally, the temperature was brought down to 20°C.

Purification of DNA origami

Self-assembled rectangular DNA origami plates underwent 3 cycles of PEG-induced precipitation [83] to remove excess staples. To that end, DNA origami samples were brought to a volume of 250 μL with folding buffer (1× TE + 12.5 mM $MgCl_2$) and mixed 1:1 to a final volume of 500 μL with a solution containing 8000 Da polyethylene glycol (PEG8000, Sigma-Aldrich) at 15% (w/v) in 1× TE + 505 mM NaCl. After mixing *via* tube inversion, the solution was centrifuged (16,000g) at room temperature for 25 minutes. The supernatant was discarded, the pellet was reconstituted in 250 μL folding buffer, and the solution incubated at room temperature for at least 30 minutes before proceeding with the next precipitation cycle. After 3 cycles, the origami pellet was reconstituted to a final concentration of 10 nM and stored at room temperature in the dark to prevent photobleaching.

Vesicle Functionalisation with DNA line-actants

Anchoring modules were incubated with vesicles (16.7 μL of DNA + 9.2 μL GUVs) with 57.4 μL of buffer resulting in an iso-osmolar mixture. Purified DNA origami tiles were heated up to ∼ 40°C for 10 minutes, followed by gentle vortexing to destabilise aggregates, and 8.35 μL were mixed with a second correction buffer (10 μL). The mixture was gently added to the GUVs decorated with anchoring modules, resulting in an iso-osmolar solution (1× TE + 99.2 mM NaCl + 0.8 mM $MgCl_2$ + 86.2 mM Glucose) that was left under rotation for at least 3 hours to allow for origami hybridisation to the anchor modules. In all cases, the nominal anchor concentration was in ∼ 1.5× excess of the origami binding capacity. Finally, the GUVs were placed in silicone wells for imaging, and allowed to sink for at least ∼15 minutes before imaging.

Agarose Gel Electrophoresis (AGE)

Agarose gels were prepared at 2% (weight) in Tris-Borate-EDTA (TBE, Sigma-Aldrich, 89 mM Tris-borate, 2 mM EDTA, pH 8.3) buffer. The mixture was dissolved *via* heating. Subsequently, SYBR Safe DNA gel stain (Invitrogen) was added at 0.1% (volume) mixed through gentle swirling, and was later casted to a thickness of approximately 5 mm. After setting for 1 hour, the gel was placed in an electrophoresis chamber and covered with TBE. 20 μL of annealed origami samples were loaded onto the gel alongside a DNA reference ladder (100 bp GeneRuler, Thermo Scientific). Control samples included origami staples and annealed scaffold. The electrophoresis chamber was placed on ice, and a potential of 75 V (3.75 V cm^{-1}) was applied for 90 minutes. Finally, the gel was imaged with a GelDoc-It system containing a UV lamp for illumination.

Fluorescence Microscopy of GUVs

Clean glass slides (15 min sonication cycles Hellmanax III 2%/isopropanol/MilliQ water) were passivated by covering with a solution containing bovine serum albumin (BSA) at 0.1% (w/v) and incubating in a pre-heated oven ($T > 60°$C) for an hour. Excess of BSA was removed with thorough rinsing with milli Q water. Silicone incubation chambers (Sigma-Aldrich) were stuck to passivated slides and sealed with DNAse-free tape to prevent evaporation.

Confocal imaging was performed at 1400 Hz, averaging over 10 frames, with a Leica TCS SP5 confocal microscope and an HC PL APO CORR CS 40× / 0.85 dry objective from Leica. Alexa488 (excitation maximum - 495 nm; emission maximum - 520 nm) signal was acquired exciting with an Ar-ion laser (488 nm).

Epifluorescence microscopy was carried out at 10 frames per second using a home-built Nikon Eclipse Ti-E inverted microscope equipped with a 40× objective lens from Nikon (Plan APO λ, NA 0.95) and a Grasshopper3 GS3-U3-23S6M camera from Point Gray Research. Illumination in this set-up was provided by single-colour light emitting diodes (LEDs) through a filter set for Texas Red.

Atomic Force Microscopy

Atomic Force Microscopy (AFM) was used to confirm the correct assembly of DNA origami plates. After the temperature ramp, $10\,\mu$L of DNA origami samples at $\sim 1\,$nM ($1\times$ TE + $12.5\,$mM MgCl$_2$) were casted on top of a freshly cleaved mica sheet, which was previously fixed onto a microscope slide and cleaved with sticky-tape. The sample was incubated for 10 minutes before two cycles of washing. These consisted of adding $300\,\mu$L of ultrapure water on top of the mica sheet, followed by drying under a gentle nitrogen flow for 3 minutes. Micrographs were acquired using a MFP-3D Infinity AFM (Asylum Research) in Dry Tapping Mode. AFM silicon probes (BudgetSensors) bearing an aluminum reflex coating had a nominal frequency of $\sim 300\,$kHz and a stiffness of $40\,\mathrm{N}\cdot\mathrm{m}^{-1}$. Data processing was performed with Gwyddion [84] by levelling the data and applying mean plane subtraction and row alignment.

DATA AVAILABILITY

Data in support of this work are available from the corresponding authors.

CODE AVAILABILITY

MATLAB scripts used to analyse data are available from the corresponding authors.

ACKNOWLEDGMENTS

R.R.S. acknowledges support from the EPSRC CDT in Nanoscience and Nanotechnology (NanoDTC, Grant No. EP/L015978/1), the Mexican National Council for Science and Technology and the Cambridge Trust. L.D.M. acknowledges support from a Royal Society University Research Fellowship (UF160152). R.R.S. and L.D.M. also acknowledge funding from the Royal Society Research Fellows Enhanced Research Expenses (RF/ERE/210029) and from the European Research Council (ERC) under the Horizon 2020 Research and Innovation Programme (ERC-STG No 851667 NANOCELL). The authors acknowledge computational resources provided by the Consortium des Équipements de Calcul Intensif (CÉCI), funded by the Fonds de la Recherche Scientifique de Belgique (F.R.S.-FNRS) under Grant No. 2.5020.11 and by the Walloon Region.

AUTHOR CONTRIBUTIONS

R.R.S and L.D.M designed the research and experimental implementation. R.R.S. carried out all experimental work and data analysis. R.R.S., B.M.M., and L.D.M. developed the numerical model. B.M.M. developed the simulation model and strategy with help from R.R.S., L.D.M., and P.C.. R.R.S. and L.D.M. wrote the manuscript. All authors discussed the results and edited the manuscript.

COMPETING INTERESTS

The authors declare no competing interests.

---

[*] rmr44@cam.ac.uk

[†] ld389@cam.ac.uk

[1] Alberts, B. *Molecular biology of the cell.* (New York : Garland Science, 2017., 2017), sixth edit edn.

[2] Veatch, S. L. *et al.* Critical Fluctuations in Plasma Membrane Vesicles. *ACS Chem. Biol.* **3**, 287–293 (2008).

[3] Baumgart, T. *et al.* Large-scale fluid/fluid phase separation of proteins and lipids in giant plasma membrane vesicles. *Proc. Natl. Acad. Sci. U. S. A.* **104**, 3165 LP – 3170 (2007).

[4] Honerkamp-Smith, A. R., Veatch, S. L. & Keller, S. L. An introduction to critical points for biophysicists; observa-

tions of compositional heterogeneity in lipid membranes. *Biochim. Biophys. Acta Biomembr.* **1788**, 53–63 (2009).

[5] Veatch, S. L. & Cicuta, P. Critical Lipidomics: The Consequences of Lipid Miscibility in Biological Membranes BT - Physics of Biological Membranes. In Bassereau, P. & Sens, P. (eds.) *Physics of Biological Membranes*, 141–168 (Springer International Publishing, Cham, 2018).

[6] Shaw, T. R., Ghosh, S. & Veatch, S. L. Critical Phenomena in Plasma Membrane Organization and Function. *Annu. Rev. Phys. Chem.* **72**, 51–72 (2021).

[7] Cammarota, E. *et al.* Criticality of plasma membrane lipids reflects activation state of macrophage cells. *J. R. Soc. Interface* **17**, 20190803 (2020).

[8] Gray, E. M., Díaz-Vázquez, G. & Veatch, S. L. Growth Conditions and Cell Cycle Phase Modulate Phase Transition Temperatures in RBL-2H3 Derived Plasma Membrane Vesicles. *PLOS ONE* **10**, e0137741 (2015).

[9] Frechin, M. *et al.* Cell-intrinsic adaptation of lipid composition to local crowding drives social behaviour. *Nature* **523**, 88–91 (2015).

[10] Ernst, R., Ballweg, S. & Levental, I. Cellular mechanisms of physicochemical membrane homeostasis. *Curr. Opin. Cell Biol.* **53**, 44–51 (2018).

[11] Weise, K., Triola, G., Brunsveld, L., Waldmann, H. & Winter, R. Influence of the Lipidation Motif on the Partitioning and Association of N-Ras in Model Membrane Subdomains. *J. Am. Chem. Soc.* **131**, 1557–1564 (2009).

[12] Weise, K., Triola, G., Janosch, S., Waldmann, H. & Winter, R. Visualizing association of lipidated signaling proteins in heterogeneous membranes Partitioning into subdomains, lipid sorting, interfacial adsorption, and protein association. *Biochim. Biophys. Acta Biomembr.* **1798**, 1409–1417 (2010).

[13] Weise, K. *et al.* Membrane-Mediated Induction and Sorting of K-Ras Microdomain Signaling Platforms. *J. Am. Chem. Soc.* **133**, 880–887 (2011).

[14] Lin, X., Gorfe, A. A. & Levental, I. Protein Partitioning into Ordered Membrane Domains: Insights from Simulations. *Biophys. J.* **114**, 1936–1944 (2018).

[15] Nicolini, C. *et al.* Visualizing Association of N-Ras in Lipid Microdomains: Influence of Domain Structure and Interfacial Adsorption. *J. Am. Chem. Soc.* **128**, 192–201 (2006).

[16] García-Sáez, A. J., Chiantia, S. & Schwille, P. Effect of Line Tension on the Lateral Organization of Lipid Membranes. *J. Biol. Chem.* **282**, 33537–33544 (2007).

[17] García-Sáez, A. J., Chiantia, S., Salgado, J. & Schwille, P. Pore Formation by a Bax-Derived Peptide: Effect on the Line Tension of the Membrane Probed by AFM. *Biophys. J.* **93**, 103–112 (2007).

[18] Schmid, F. Physical mechanisms of micro- and nanodomain formation in multicomponent lipid membranes. *Biochim. Biophys. Acta Biomembr.* **1859**, 509–528 (2017).

[19] Lingwood, D. & Simons, K. Lipid Rafts As a Membrane-Organizing Principle. *Science* **327**, 46 LP – 50 (2010).

[20] Simons, K. & Toomre, D. Lipid rafts and signal transduction. *Nat. Rev. Mol. Cell Biol.* **1**, 31 (2000).

[21] Shelby, S. A., Castello-Serrano, I., Wisser, K. C., Levental, I. & Veatch, S. L. Membrane phase separation drives organization at B cell receptor clusters. *bioRxiv* (2021).

[22] Booth, A., Marklew, C., Ciani, B. & Beales, P. A. The influence of phosphatidylserine localisation and lipid phase on membrane remodelling by the ESCRT-II/ESCRT-III complex. *Faraday Discussions* (2020).

[23] Kim, J. H., Singh, A., Del Poeta, M., Brown, D. A. & London, E. The effect of sterol structure upon clathrin-mediated and clathrin-independent endocytosis. *J. Cell Sci.* **130**, 2682–2695 (2017).

[24] Buddingh', B. C. & van Hest, J. C. M. Artificial Cells: Synthetic Compartments with Life-like Functionality and Adaptivity. *Accounts of Chemical Research* **50**, 769–777 (2017).

[25] Noireaux, V., Maeda, Y. T. & Libchaber, A. Development of an artificial cell, from self-organization to computation and self-reproduction. *Proceedings of the National Academy of Sciences of the United States of America* **108**, 3473 LP – 3480 (2011).

[26] Emir Diltemiz, S. *et al.* Use of artificial cells as drug carriers. *Mater. Chem. Front.* **5**, 6672–6692 (2021).

[27] Zhang, Y., Ruder, W. C. & LeDuc, P. R. Artificial cells: building bioinspired systems using small-scale biology. *Trends in Biotechnology* **26**, 14–20 (2008).

[28] Xu, C., Hu, S. & Chen, X. Artificial cells: from basic science to applications. *Materials Today* **19**, 516–532 (2016).

[29] Trantidou, T. *et al.* Engineering Compartmentalized Biomimetic Micro- and Nanocontainers. *ACS Nano* **11**, 6549–6565 (2017).

[30] Hindley, J. W., Law, R. V. & Ces, O. Membrane functionalization in artificial cell engineering. *SN Appl. Sci.* **2**, 593 (2020).

[31] Hindley, J. W. *et al.* Building a synthetic mechanosensitive signaling pathway in compartmentalized artificial cells. *Proc. Natl. Acad. Sci. U. S. A.* **116**, 16711 LP – 16716 (2019).

[32] Hindley, J. W. *et al.* Light-triggered enzymatic reactions in nested vesicle reactors. *Nat. Commun.* **9**, 1093 (2018).

[33] Lee, K. Y. *et al.* Photosynthetic artificial organelles sustain and control ATP-dependent reactions in a protocellular system. *Nat. Biotechnol.* **36**, 530–535 (2018).

[34] Altamura, E. *et al.* Highly oriented photosynthetic reaction centers generate a proton gradient in synthetic protocells. *Proc. Natl. Acad. Sci. U. S. A.* **114**, 3837–3842 (2017).

[35] Litschel, T., Ramm, B., Maas, R., Heymann, M. & Schwille, P. Beating Vesicles: Encapsulated Protein Oscillations Cause Dynamic Membrane Deformations. *Angew. Chem. Int. Ed.* **57**, 16286–16290 (2018).

[36] Beales, P. A. & Vanderlick, T. K. Application of nucleic acid–lipid conjugates for the programmable organisation of liposomal modules. *Adv. Colloid Interface Sci.* **207**, 290–305 (2014).

[37] Langecker, M., Arnaut, V., List, J. & Simmel, F. C. DNA Nanostructures Interacting with Lipid Bilayer Membranes. *Acc. Chem. Res.* **47**, 1807–1815 (2014).

[38] Rubio-Sánchez, R., Fabrini, G., Cicuta, P. & Di Michele, L. Amphiphilic DNA nanostructures for bottom-up synthetic biology. *Chem. Commun.* **57**, 12725–127405 (2021).

[39] Sobota, D., Joshi, H., Ohmann, A., Aksimentiev, A. & Keyser, U. F. Tailoring Interleaflet Lipid Transfer with a DNA-based Synthetic Enzyme. *Nano Lett.* **20**, 4306–4311 (2020).

[40] Ohmann, A. *et al.* A synthetic enzyme built from DNA flips 107 lipids per second in biological membranes. *Nat. Commun.* **9**, 2426 (2018).

[41] Morzy, D. *et al.* Cations regulate membrane-attachment and functionality of DNA nanostructures. *J. Am. Chem. Soc.* **143**, 7358–7367 (2021).

[42] Fragasso, A. *et al.* Reconstitution of Ultrawide DNA Origami Pores in Liposomes for Transmembrane Transport of Macromolecules. *ACS Nano* **15**, 12768–12779 (2021).

[43] Diederichs, T. *et al.* Synthetic protein-conductive membrane nanopores built with DNA. *Nat. Commun.* **10**, 5018 (2019).

[44] Amjad, O. A., Mognetti, B. M., Cicuta, P. & Di Michele, L. Membrane Adhesion through Bridging by Multimeric Ligands. *Langmuir* **33**, 1139–1146 (2017).

[45] Mognetti, B. M., Cicuta, P. & Di Michele, L. Programmable interactions with biomimetic DNA linkers at fluid membranes and interfaces. *Rep. Prog. Phys.* **82**, 116601 (2019).

[46] Parolini, L., Kotar, J., Di Michele, L. & Mognetti, B. M. Controlling Self-Assembly Kinetics of DNA-Functionalized Liposomes Using Toehold Exchange Mechanism. *ACS Nano* **10**, 2392–2398 (2016).

[47] Parolini, L. *et al.* Volume and porosity thermal regulation in lipid mesophases by coupling mobile ligands to soft membranes. *Nat. Commun.* **6**, 5948 (2015).

[48] Beales, P. A., Nam, J. & Vanderlick, T. K. Specific adhesion between DNA-functionalized “Janus” vesicles: size-limited clusters. *Soft Matter* **7**, 1747–1755 (2011).

[49] Kaufhold, W. T., Brady, R. A., Tuffnell, J. M., Cicuta, P. & Di Michele, L. Membrane Scaffolds Enhance the Responsiveness and Stability of DNA-Based Sensing Circuits. *Bioconjug. Chem.* (2019).

[50] Walczak, M. *et al.* Responsive core-shell dna particles trigger lipid-membrane disruption and bacteria entrapment. *Nat. Commun.* 4743 (2021).

[51] Journot, C. M. A., Ramakrishna, V., Wallace, M. I. & Turberfield, A. J. Modifying Membrane Morphology and Interactions with DNA Origami Clathrin-Mimic Networks. *ACS Nano* **13**, 9973–9979 (2019).

[52] Franquelim, H. G., Khmelinskaia, A., Sobczak, J.-P., Dietz, H. & Schwille, P. Membrane sculpting by curved DNA origami scaffolds. *Nat. Commun.* **9**, 811 (2018).

[53] Franquelim, H. G., Dietz, H. & Schwille, P. Reversible membrane deformations by straight DNA origami filaments. *Soft Matter* **17**, 276–287 (2021).

[54] Rubio-Sánchez, R., Barker, S. E., Walczak, M., Cicuta, P. & Di Michele, L. A Modular, Dynamic, DNA-Based Platform for Regulating Cargo Distribution and Transport between Lipid Domains. *Nano Lett.* **21**, 2800–2808 (2021).

[55] Schade, M. *et al.* Remote Control of Lipophilic Nucleic Acids Domain Partitioning by DNA Hybridization and Enzymatic Cleavage. *J. Am. Chem. Soc.* **134**, 20490–20497 (2012).

[56] Czogalla, A. *et al.* Switchable domain partitioning and diffusion of DNA origami rods on membranes. *Faraday Discuss.* **161**, 31–43 (2013).

[57] Schindelin, J. *et al.* Fiji: an open-source platform for biological-image analysis. *Nat. Methods* **9**, 676–682 (2012).

[58] Schnitzbauer, J., Strauss, M. T., Schlichthaerle, T., Schueder, F. & Jungmann, R. Super-resolution microscopy with DNA-PAINT. *Nat. Protoc.* **12**, 1198–1228 (2017).

[59] Strauss, M. T., Schueder, F., Haas, D., Nickels, P. C. & Jungmann, R. Quantifying absolute addressability in DNA origami with molecular resolution. *Nat. Commun.* **9**, 1600 (2018).

[60] Clowsley, A. H. *et al.* Detecting Nanoscale Distribution of Protein Pairs by Proximity-Dependent Super-resolution Microscopy. *J. Am. Chem. Soc.* **142**, 12069–12078 (2020).

[61] Clowsley, A. H. *et al.* Repeat DNA-PAINT suppresses background and non-specific signals in optical nanoscopy. *Nat. Commun.* **12**, 501 (2021).

[62] Honerkamp-Smith, A. R. *et al.* Line Tensions, Correlation Lengths, and Critical Exponents in Lipid Membranes Near Critical Points. *Biophys. J.* **95**, 236–246 (2008).

[63] Veatch, S. L. & Keller, S. L. Separation of Liquid Phases in Giant Vesicles of Ternary Mixtures of Phospholipids and Cholesterol. *Biophys. J.* **85**, 3074–3083 (2003).

[64] Landau, D. & Binder, K. *A guide to Monte Carlo simulations in statistical physics* (Cambridge university press, 2021).

[65] Stanich, C. *et al.* Coarsening Dynamics of Domains in Lipid Membranes. *Biophysical Journal* **105**, 444–454 (2013).

[66] Zhang, D. Y. & Winfree, E. Control of DNA Strand Displacement Kinetics Using Toehold Exchange. *Journal of the American Chemical Society* **131**, 17303–17314 (2009).

[67] Zhang, D. Y. & Seelig, G. Dynamic DNA nanotechnology using strand-displacement reactions. *Nature Chemistry* **3**, 103 (2011).

[68] Ursell, T. S., Klug, W. S. & Phillips, R. Morphology and interaction between lipid domains. *Proceedings of the National Academy of Sciences* **106**, 13301–13306 (2009).

[69] Kretschmer, S., Ganzinger, K. A., Franquelim, H. G. & Schwille, P. Synthetic cell division via membrane-transforming molecular assemblies. *BMC Biology* **17**, 43 (2019).

[70] Staneva, G., Angelova, M. I. & Koumanov, K. Phospholipase A2 promotes raft budding and fission from giant liposomes. *Chem. Phys. Lipids* **129**, 53–62 (2004).

[71] Steinkühler, J. *et al.* Controlled division of cell-sized vesicles by low densities of membrane-bound proteins. *Nature Communications* **11**, 905 (2020).

[72] Reinhard Lipowsky. Budding of membranes induced by intramembrane domains. *J. Phys. II France* **2**, 1825–1840 (1992).

[73] Dreher, Y., Jahnke, K., Bobkova, E., Spatz, J. P. & Göpfrich, K. Division and Regrowth of Phase-Separated Giant Unilamellar Vesicles**. *Angewandte Chemie International Edition* **60**, 10661–10669 (2021).

[74] Carman, P. J. & Dominguez, R. BAR domain proteins-a linkage between cellular membranes, signaling pathways, and the actin cytoskeleton. *Biophysical reviews* **10**, 1587–1604 (2018).

[75] Chiaruttini, N. *et al.* Relaxation of Loaded ESCRT-III Spiral Springs Drives Membrane Deformation. *Cell* **163**, 866–879 (2015).

[76] Lu, Y. & Liu, J. Functional DNA nanotechnology: emerging applications of DNAzymes and aptamers. *Curr. Opin. Biotechnol.* **17**, 580–588 (2006).

[77] Fabrini, G., Minard, A., Brady, R. A., Di Antonio, M. & Di Michele, L. Cation-Responsive and Photocleavable Hydrogels from Noncanonical Amphiphilic DNA Nanos-

tructures. *Nano Lett.* **22**, 602–611 (2022).

[78] Del Grosso, E., Ragazzon, G., Prins, L. J. & Ricci, F. Back Cover: Fuel-Responsive Allosteric DNA-Based Aptamers for the Transient Release of ATP and Cocaine (Angew. Chem. Int. Ed. 17/2019). *Angew. Chem. Int. Ed.* **58**, 5772 (2019).

[79] Hernández-Ainsa, S. *et al.* Controlling the Reversible Assembly of Liposomes through a Multistimuli Responsive Anchored DNA. *Nano Lett.* **16**, 4462–4466 (2016).

[80] Angelova, M. I. & Dimitrov, D. S. Liposome electroformation. *Faraday Discuss. Chem. Soc.* **81**, 303–311 (1986).

[81] Zadeh, J. N. *et al.* NUPACK: Analysis and design of nucleic acid systems. *J. Comput. Chem.* **32**, 170–173 (2010).

[82] Rothemund, P. W. K. Folding DNA to create nanoscale shapes and patterns. *Nature* **440**, 297 (2006).

[83] Stahl, E., Martin, T. G., Praetorius, F. & Dietz, H. Facile and Scalable Preparation of Pure and Dense DNA Origami Solutions. *Angew. Chem. Int. Ed* **53**, 12735–12740 (2014).

[84] Nečas, D. & Klapetek, P. Gwyddion: an open-source software for SPM data analysis. *Cent. Eur. J. Phys.* **10**, 181–188 (2012).